

StructuredField: Unifying Structured Geometry and Radiance Field

Kaiwen Song Jinkai Cui Zherui Qiu Juyong Zhang
University of Science and Technology of China

Abstract

Recent point-based differentiable rendering techniques have achieved significant success in high-fidelity reconstruction and fast rendering. However, due to the unstructured nature of point-based representations, they are difficult to apply to modern graphics pipelines designed for structured meshes, as well as to a variety of simulation and editing algorithms that work well with structured mesh representations. To this end, we propose StructuredField, a novel representation that achieves both a structured geometric representation of the reconstructed object and a high-fidelity rendering reconstruction of the object. We employ structured tetrahedral meshes to represent the reconstructed object. We reparameterize the geometric parameters of the tetrahedral mesh into the geometric shape parameters of a 3D Gaussians, thereby achieving differentiable high-fidelity rendering of the tetrahedral mesh. We propose a novel inversion-free homeomorphism to constrain the optimization of the tetrahedral mesh, which strictly guarantees that the tetrahedral mesh remains both inversion-free and self-intersection-free during the optimization process and the final result. Based on our proposed StructuredField, we achieve high-quality structured meshes and high-fidelity reconstruction. We also demonstrate the applicability of our representation to various applications such as physical simulation and deformation. Project page: <https://structuredfield.github.io>

1. Introduction

Photorealistic and real-time rendering of 3D scenes is a central pursuit in computer graphics, both in academic research and practical applications. Traditional 3D representations, such as meshes [9, 19, 34] and point clouds [47, 64], facilitate real-time rendering through rasterization techniques that align with modern GPU rendering architectures. Nevertheless, these methods frequently produce low-quality rendering, exhibiting missing geometric details and blurry artifacts. In contrast, emerging differentiable volumetric rendering methods [5, 11, 41], including neural radiance fields [39], demonstrate the capability to reconstruct 3D

scenes in an end-to-end manner using multi-view images, thus achieving high fidelity and maintaining intricate details. However, the reliance on ray tracing-based rendering pipelines and the necessity for extensive sampling points pose challenges to rapid rendering in NeRF variants.

Recently, advancements in point-based differentiable rendering techniques [18, 22, 23, 30] have demonstrated notable success in enhancing both rendering speed and high-fidelity reconstruction by leveraging smooth primitives alongside rasterization-based pipeline. Although point-based rendering techniques offer numerous advantages, they inherently represent scenes as unstructured point clouds. In contrast, contemporary graphics pipelines are designed for structured representations, such as polygonal meshes, which are increasingly favored in a variety of applications, including animation [25, 49], physical simulation [3, 4, 35] and editing [65, 68]. The lack of a representation for the structure of objects within point-based rendering methods significantly constrains their broader applications.

In this study, our aim is to bridge the gap between recent high-fidelity differentiable point-based representations and traditional graphics pipelines that are tailored for structured meshes. To achieve this, we introduce a structured representation that facilitates both high-fidelity rendering and the recovery of near-surface structures. Specifically, we use tetrahedral mesh as the fundamental representation. Compared to triangular mesh, tetrahedral mesh is better suited for volumetric data and has been widely utilized in volume rendering [36, 58, 61]. We leverage point-based 3D representations as differentiable renderers and employ differentiable mappings to reparameterize primitive parameters with the attributes of tetrahedral mesh. Thereby, we enable the optimization of tetrahedral mesh parameters in a differentiable manner and achieve high-fidelity reconstruction.

However, we find that directly optimizing tetrahedral mesh without constraints leads to anomalous topological structures. To mitigate this challenge, we analyze two main causes of mesh anomalies: self intersections and element inversions. We employ homeomorphic mappings [8, 12] to prevent self intersections and introduce permutations to ensure that the Jacobian determinant remains positive, thereby preventing element inversions in mesh. By utilizing

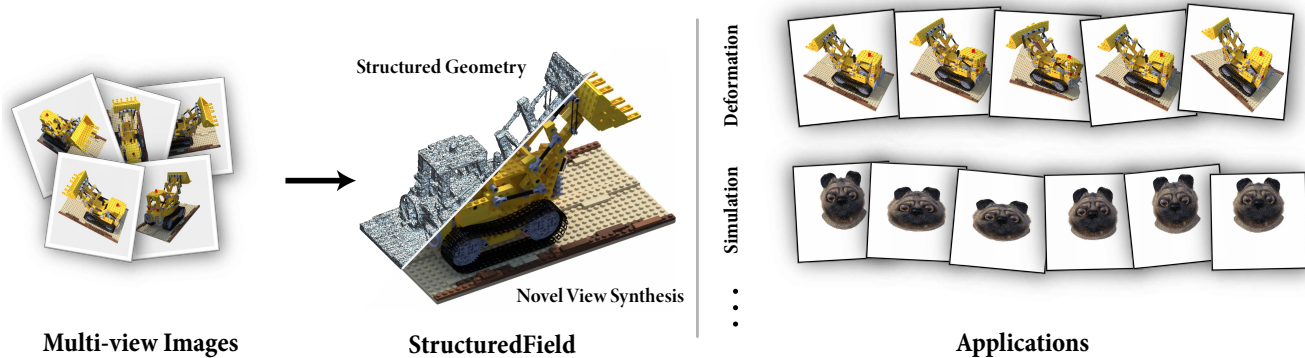


Figure 1. **StructuredField** represents and reconstructs scene using a structured tetrahedral mesh. This novel structured 3D representation enables a variety of applications, including physical simulations, deformations, and more.

this orientation-preserving homeomorphism as a constraint within the feasible solution space, we can prevent the occurrence of self intersections or inversions in the tetrahedral mesh during the optimization process.

Through comprehensive experimentation, we demonstrate that our approach achieves rendering quality comparable to or even exceeding that of recent point-based rendering techniques. Furthermore, our representation can be seamlessly integrated into various applications like physics simulation and deformation without necessitating algorithmic redesigns or extensive modifications. Our primary contributions can be summarized as:

- We introduce a novel 3D structured representation that employs reparameterization to make tetrahedral mesh differentiable, facilitating high-fidelity scene reconstruction.
- We propose a novel invertible network architecture specifically designed to represent orientation-preserving homeomorphisms, which ensures that the tetrahedral mesh remains inversion-free and self-intersection-free during optimization.
- StructuredField can achieve high quality geometry and rendering reconstruction while supporting physics simulation and deformation without any modifications.

2. Related Work

2.1. 3D Reconstruction

Reconstructing 3D scenes from multi-view images is a longstanding problem in both computer graphics and computer vision. Traditional 3D reconstruction techniques include Structure-from-Motion (SfM) pipelines [2, 13] to estimate camera poses and obtain sparse point clouds, followed by surface reconstruction through dense multi-view stereo [15, 16, 28]. These methods rely on hand-crafted features to acquire fine textures and geometry, and struggle to reconstruct view-dependent colors. Significant advancements have been achieved in NVS, particularly since the

introduction of Neural Radiance Fields (NeRF) [39]. The original NeRF represents the scene as an MLP, which maps positional encodings of spatial locations and directions to attributes including color and density, and utilizes volume rendering process to achieve realistic rendering. Various works have enhanced the performance of NeRF [5, 7, 41] or extended them to large scenes [6, 50]. More recently, 3DGS [30] optimizes anisotropic 3D Gaussian primitives, demonstrating real-time photorealistic reconstruction results. This method has been quickly extended to multiple domains [29, 33, 51, 60]. Despite these successes, point-based representations are unstructured, limiting their further applications. In this paper, we demonstrate detailed reconstruction while maintaining a structured tetrahedral mesh, and showcase its subsequent applications.

2.2. Mesh-based Representation

Explicit representations have served as a cornerstone within 3D modeling and computer graphics for decades [59]. Conventional geometric representations like point clouds, voxels and polygonal meshes have been extensively revisited in the context of 3D deep learning. Polygonal meshes are particularly attractive due to their structured geometry and efficient rendering properties. Recently, differentiable rendering methods [34, 43] leveraging mesh representations have enabled the production of high-quality renderings. However, the optimization processes inherent to mesh representations are often hampered by rigid topological constraints, resulting in limited flexibility and reduced capacity to accurately depict realistic appearances. Our method integrates inversion-free mapping to effectively regulate and maintain structural integrity during the mesh optimization process while ensuring high quality reconstruction, addressing these limitations.

On the other hand, NeRF [38] has attracted considerable attention due to their ability to deliver high-fidelity renderings. Substantial research has focused on integrating im-

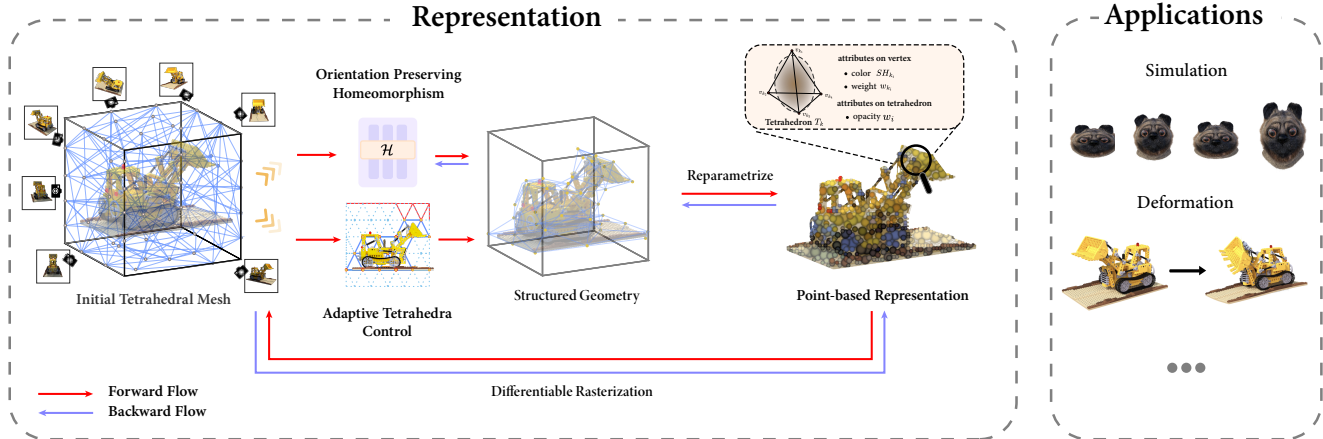


Figure 2. **Overview of StructuredField.** Given multi-view images as input, we reconstruct the 3D scene using a structured tetrahedral mesh. We use an orientation-preserving homeomorphism to maintain the inversion-free structured geometry of the tetrahedral mesh during optimization. Additionally, parameters of tetrahedral mesh are reparameterized into the corresponding 3D Gaussian parameters, enabling differentiable optimization. Finally, we use differentiable rasterization to render images from the given viewpoints. Based on our structured mesh representation, we can further apply the model to physical simulations, deformation, and other applications.

PLICIT methods with mesh structures to extend and refine NeRF [54]. For instance, some approaches [52, 53, 57] utilize meshes to constrain the sampling regions within an adaptively learned narrow band of two explicit meshes. On the other hand, Tetra-NeRF [31, 46] employs tetrahedral mesh as feature grids to accelerate the training process. Additionally, leveraging the fast rendering capabilities of meshes, Baked SDF and its variants [45, 63] have baked radiance fields into meshes to facilitate real-time rendering. Mesh representations have also been pivotal in the deformation of radiance fields. NeRFShop and Cage-NeRF [24, 42] using meshes as cages to drive the deformation of radiance fields.

Recently, point-based representations [22, 23, 30] have emerged, utilizing smooth primitives to represent radiance fields and employing rasterization techniques to accelerate rendering. In the subsequent works, Mani-gs and GaMes [17] employ high-quality triangle meshes or triangle soups as proxies, binding primitives to the triangle mesh to drive the deformation of 3D Gaussians. Additionally, VR-GS [26] and D3GA [67] adopt tetrahedral mesh as proxies to facilitate the deformation of objects. However, these methods directly bind the mesh to Gaussians without optimizing the positions of the mesh vertices. As a result, any imperfections in the initial mesh can significantly degrade the final reconstruction quality. In contrast, our method reparameterizes Gaussians with tetrahedral mesh vertices and optimizes these vertices, thereby allowing for high-quality reconstruction.

2.3. Inversion-free Mesh Optimization

Maintaining mesh quality during the optimization process remains a challenging problem. Element inversion is a major factor causing mesh quality issues [14]. Traditional methods [44, 48] impose constraints on the Jacobian of the mapping during optimization to ensure the Jacobian remains positive, thereby enforcing that the mapping is orientation-preserving. In addition to being inversion-free, intersection-free boundaries are also necessary during the optimization. This is typically achieved by constraining the mapping to be bijective. Traditional methods [27, 40] introduce scaffold meshes to convert the globally overlap-free constraint into a locally flip-free condition. Recently, invertible networks [8, 12] offer another solution, leading to their widespread adoption in recent 3D deformation tasks. For instance, NDR [10] and Cadex [32] employ invertible networks to model the motion of objects, thereby achieving dynamic object reconstruction. NFGP [62] utilizes invertible networks to perform geometric processing on implicit surfaces. Compared to these methods, we propose a novel invertible network that implicitly and strictly constrains the mapping to be inversion-free and intersection-free, and apply it during the optimization process to guarantee the mesh quality.

3. Method

Given multi-view posed images of a scene, our primary objective is to reconstruct it with high fidelity, capturing not only its geometric details but also the structures near its surface. This enables seamless integration of the reconstructed 3D scene into existing computer graphics pipelines, such

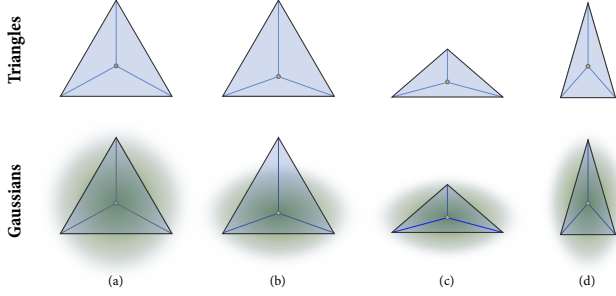


Figure 3. **2D illustration of reparameterizing Gaussians.** In (a), (c), and (d), all vertex weights are equal, $w_1 = w_2 = w_3 = 1.0$. In (b), the bottom vertices v_2 and v_3 have higher weights, $w_1 = 0.1, w_2 = w_3 = 1.0$.

as those used for rendering, animation, physical simulation, and deformation. To this end, we first introduce a novel tetrahedral mesh-based 3D representation that is structurally organized and facilitates differentiable optimization (Sec. 3.1). The mesh is optimized using orientation-preserving homeomorphism to ensure high-quality structured geometry (Sec. 3.2). An overview of our representation and reconstruction pipeline is shown in Fig. 2.

Given a tetrahedral mesh $\mathcal{M} = (\mathcal{V}, \mathcal{T})$, where $\mathcal{V} = \{v_i\}_{i=1}^N$ represents the set of vertices, $\mathcal{T} = \{T_k\}_{k=1}^K$ is the set of tetrahedron. Each tetrahedron $T_k \in \mathcal{T}$ is defined by four vertices $\{v_{k_1}, v_{k_2}, v_{k_3}, v_{k_4}\}$. Tetrahedral mesh is generally challenging to render in a differentiable manner due to their discrete, non-smooth nature.

To address this limitation, we build upon recent point-based differentiable rendering techniques, such as 3D Gaussian Splatting (3DGS) [30], 2D Gaussian Splatting (2DGS) [22], and convex splatting [18]. In our method, we establish a one-to-one correspondence between each tetrahedron and a primitive, using a differentiable reparameterization function $\mathbf{F}_r(\cdot)$ to map the parameters T_k of the tetrahedron to the parameters Θ_k of the primitive:

$$\Theta_k = \mathbf{F}_r(T_k). \quad (1)$$

Gradients are propagated back to the parameters of tetrahedra through the differentiable reparameterization function, enabling the optimization of vertex positions and associated attributes in a fully differentiable framework. In the following, we demonstrate how the parameters of 3DGS can be reparameterized using the parameters of a tetrahedral mesh.

3.1. Representation of StructuredField

Reparameterize 3D Gaussians 3DGS [30] represent a scene with a set of 3D Gaussians $\mathcal{G} = \{g_k\}_{k=1}^K$, where each Gaussian g_k encodes the following attributes: mean $\mu_k \in \mathbb{R}^3$, scales $s_k \in \mathbb{R}^3$, rotation $r_k \in \mathbb{R}^4$, color $c_k \in \mathbb{R}^3$, and opacity $o_k \in \mathbb{R}$. In our representation, each tetrahedron

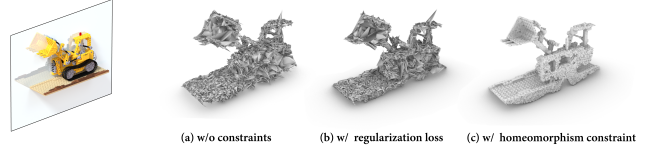


Figure 4. **Visualization of mesh optimization using different methods.** We retain tetrahedra in the region where $y > 0$ to better visualize the internal structure of the tetrahedral mesh. The experimental setup can be found in Sec. 4.1. The regularization loss used in the figure is \mathcal{L}_{sv} .

T_k contains four vertices with positions $\{\mathbf{v}_{k_i}\}_{i=1}^4$, spherical harmonic coefficients $\{\mathbf{SH}_{k_i}\}_{i=1}^4$, and weights $\{w_{k_i}\}_{i=1}^4$. We adopt a PCA-style [1] approach to convert these vertices and their attributes into a 3D Gaussian. Specifically, the mean and covariance matrix of each Gaussian are computed as:

$$\begin{aligned} \boldsymbol{\mu} &= \frac{\sum_{i=1}^4 w_i \mathbf{v}_i}{\sum_{i=1}^4 w_i}, \\ \boldsymbol{\Sigma} &= \frac{\sum_{i=1}^4 w_i (\mathbf{v}_i - \boldsymbol{\mu})(\mathbf{v}_i - \boldsymbol{\mu})^\top}{\sum_{i=1}^4 w_i}. \end{aligned} \quad (2)$$

This conversion effectively captures the weighted shape of the tetrahedron, ensuring that the resulting 3D Gaussian closely resembles the original tetrahedral shape, as shown in Fig. 3.

We define the opacity attribute o_k on the tetrahedron instead of on the vertices, so the opacity of its corresponding Gaussian is equivalent to the opacity of the tetrahedron. The color of the Gaussian is obtained by a weighted average of the colors computed from the spherical harmonic function of each vertex:

$$\mathbf{c} = \frac{\sum_{i=1}^4 w_i \mathbf{c}_i}{\sum_{i=1}^4 w_i}, \quad \mathbf{c}_i = \mathbf{SH}_i(\mathbf{d}), \quad (3)$$

where \mathbf{d} is the direction from the camera center to the vertex.

After reparameterizing 3D Gaussians with tetrahedral mesh, the scene can be rendered in a differentiable manner. However, freely optimizing the tetrahedral vertices leads to low quality tetrahedral mesh, as shown in Fig. 4(a). In the following section, we introduce the orientation-preserving homeomorphism to address this issue.

3.2. Inversion-free Structured Geometry

One of our goals is to optimize the tetrahedral mesh while maintaining high-quality structure. As shown in Fig. 4(a), optimizing a tetrahedral mesh without any constraints leads to poor mesh quality. The main cause of this issue is that the vertices can freely move during the optimization of the

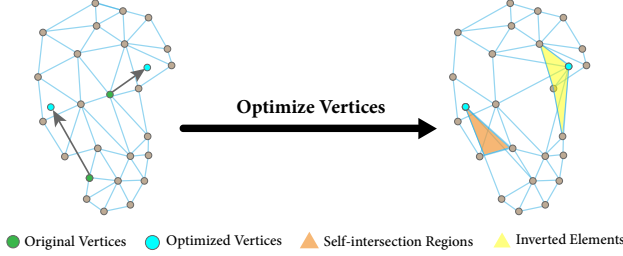


Figure 5. **Two causes leading to mesh anomalies: self intersection and element inversion.**

tetrahedral mesh. Consequently, the tetrahedral mesh suffers from self-intersections and element inversion problems, resulting in tetrahedra overlaps as shown in Fig. 5.

A naive solution is to introduce a loss function to constrain the mesh optimization process. Locally injective mapping [48] uses a barrier function to strictly prevent element inversion. However, the gradient explosion near the critical points of the barrier function makes it difficult to use directly in gradient descent-based optimization. Another approach is to apply a volume-preserving constraint $\mathcal{L}_{\text{volume}}$, or directly impose an L_1 -norm constraint on the signed volume of the optimized tetrahedra L_{sv} , making tetrahedra with negative signed volume sparse:

$$\mathcal{L}_{\text{volume}} = \frac{1}{K} \sum_{k=1}^K \|s(T_k) - s(T_k^0)\|_2, \quad (4)$$

$$\mathcal{L}_{\text{sv}} = \frac{1}{K} \sum_{k=1}^K \max(-s(T_k), 0), \quad (5)$$

where $s(T_k)$ is the signed volume of the tetrahedron T_k , T_k^0 is the initial tetrahedron. However, we found that these loss function-based constraints significantly impact the rendering quality and do not fully guarantee that the tetrahedral mesh remains reasonable structure as shown in Sec. 4.1.

Orientation-preserving Homeomorphism as constraint.

Unlike previous methods that used regularization loss, we adopt the orientation-preserving homeomorphism as a constraint, implicitly restricting the feasible region of the vertex set \mathcal{V} of the tetrahedral mesh. The two key properties of this mapping are:

- **Orientation-preserving** means that the Jacobian determinant of the mapping remains positive, which prevents element inversion during tetrahedral mesh optimization.
- **Homeomorphism** guarantees that tetrahedral mesh after optimization does not produce self-intersecting boundaries.

During optimization, both the topology \mathcal{T} and vertex positions \mathcal{V} of tetrahedral mesh are fixed. The orientation-preserving homeomorphism maps a vertex $v = [x, y, z]^T$ to

its actual position as follows:

$$v' = [x', y', z']^T = \mathcal{H}([x, y, z]^T). \quad (6)$$

We use the mapped vertices $\mathcal{V}' = \{v'_i\}$ to reparameterize the 3D Gaussians. This orientation-preserving homeomorphism can be viewed as a constraint on the feasible region of the vertices, ensuring that a valid mesh is still generated given a topology \mathcal{T} .

Real-NVP Based on these observations, we implement the orientation-preserving homeomorphism \mathcal{H} by a novel invertible network. Real-NVP [12] appears to be a reasonable network architecture, as it is bijective and ensures that the Jacobian determinant of each coupling layer remains positive. Real-NVP splits the input $x \in \mathbb{R}^D$ into two components, $x_{1:d}$ and $x_{d+1:D}$. The output of a coupling layer $x' \in \mathbb{R}^D$ follows the equations:

$$\begin{aligned} x'_{1:d} &= x_{1:d} \\ x'_{d+1:D} &= x_{d+1:D} \cdot \exp(s(x_{1:d})) + t(x_{1:d}), \end{aligned} \quad (7)$$

where $s: \mathbb{R}^d \rightarrow \mathbb{R}_+^{D-d}$ and $t: \mathbb{R}^d \rightarrow \mathbb{R}^{D-d}$ are the scale and translation functions. We denote this map of the coupling layer as $h: \mathbb{R}^D \rightarrow \mathbb{R}^D$. The Jacobian of this mapping is:

$$J_h = \begin{bmatrix} 1 & 0 \\ \frac{\partial x'_{d+1:D}}{\partial x_{1:d}} & \text{diag}[\exp(s(x_{1:d}))] \end{bmatrix}. \quad (8)$$

This is a lower triangular matrix, so its determinant is the product of the diagonal elements, which is positive. Real-NVP stacks multiple coupling layers in an alternating pattern, such that the components that are left unchanged in one coupling layer are updated in the next coupling layer. However, when we split (x, y, z) into two components: (x, z) and y , after mapping by a similar coupling layer, the Jacobian matrix is in the following form, which is not a triangular matrix, and its determinant does not remain positive.

$$J_h = \begin{bmatrix} 1 & \frac{\partial y'}{\partial x} & 0 \\ 0 & \exp(s) & 0 \\ 0 & \frac{\partial y'}{\partial z} & 1 \end{bmatrix} \quad (9)$$

Orientation-preserving Networks The above problem is caused by the fact that the input is split into discontinuous parts, resulting in the Jacobian matrix being neither an upper triangular matrix nor a lower triangular matrix. To solve this problem, we propose a permutation strategy. As shown in Fig. 6, we multiply the input by a permutation matrix P , ensuring that the input is always divided into contiguous two parts. For example, when we need to keep the x and z components unchanged and transform the y component, we apply the permutation matrix P to the input and

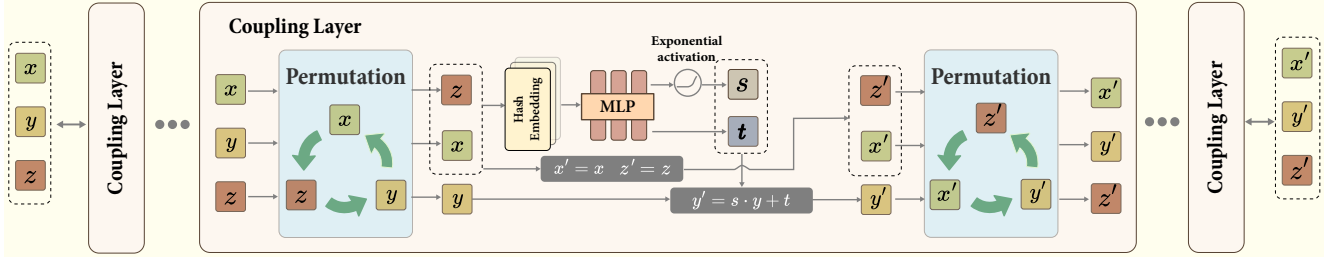


Figure 6. **Invertible neural network architecture.** By applying a permutation strategy, the input vector is divided into two contiguous parts, ensuring that the resulting Jacobian matrix is upper triangular with positive diagonal elements. This strategy guarantees that the determinant of the Jacobian is positive, thus ensuring that the mapping is inversion-free.

output. Therefore, the permuted transformation mapping $\phi : \mathbb{R}^3 \rightarrow \mathbb{R}^3$ is:

$$\phi([x, y, z]^T) = P^{-1}(h(P[x, y, z]^T))$$

$$P = \begin{bmatrix} 0 & 0 & 1 \\ 1 & 0 & 0 \\ 0 & 1 & 0 \end{bmatrix}. \quad (10)$$

Thus, the Jacobian matrix is: $J_\phi = PJ_hP^{-1}$, where J_h is the Jacobian matrix of the coupling layer h . Since J_h is an upper triangular matrix, and its diagonal elements are positive, it satisfies $\det(J_h) > 0$. As $\det(P) > 0$, it follows that $\det(J_\phi) > 0$.

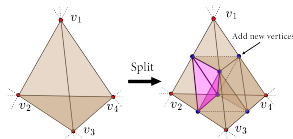
3.3. Training

Initialization We use two different initialization strategies. In the first strategy, we reconstruct the surface using NeuS2 [55], and then generate the tetrahedral mesh from the reconstructed triangle mesh using fTetWild [21]. The second is to generate a uniform tetrahedral grid within the bounding box of the scene. We conduct experiments on different initialization strategies in Sec. 4.1, which show that even with poorly initialized tetrahedral mesh, we can still achieve high-quality results.

Adaptive Tetrahedron

Control We design an adaptive control strategy to dynamically add and remove tetrahedra.

Specifically, if the gradient of a tetrahedron’s corresponding Gaussians exceeds a certain threshold δ , the tetrahedron is split. We add new vertices at the center of the tetrahedron and at the midpoints of each edge, thereby subdividing the tetrahedron into eight smaller tetrahedra. On the other hand, tetrahedra with corresponding Gaussians’ opacities less than ϵ are pruned.



Optimization Our model is trained using a loss function written as a weighted sum:

$$\mathcal{L} = \lambda_1 \mathcal{L}_1 + \lambda_2 \mathcal{L}_{\text{SSIM}} + \lambda_3 \mathcal{L}_{\text{mask}}. \quad (11)$$

The loss used for supervision of the RGB signal: \mathcal{L}_1 and $\mathcal{L}_{\text{SSIM}}$ follow 3D Gaussian splatting [30]. $\mathcal{L}_{\text{mask}}$ is designed to prevent artifacts at the object boundaries:

$$\mathcal{L}_{\text{mask}} = \|M - \hat{M}\|_1,$$

where M represents the rendered opacity, and \hat{M} represents the ground truth opacity.

4. Experiments

We first give the implementation details. The contribution analysis of proposed components is given in Sec. 4.1. Evaluations of our proposed representation, with previous state-of-the-art non-editable and editable approaches are presented in Sec. 4.2. We also show some applications of our proposed representation in Sec. 4.3

Implementation Details We set $\lambda_1 = 0.8$, $\lambda_2 = 0.2$, and $\lambda_3 = 0.5$ for training the model. We use the ReLU function to prevent the weights of the vertices from being negative, and apply the sigmoid function to ensure that the opacity stays within the range of $[0, 1)$. The gradient threshold δ for tetrahedron splitting is set to 0.0002, the same value used in 3DGS. We set the pruning threshold $\epsilon = 0.0005$ to prevent overly aggressive pruning that could result in too many isolated tetrahedra. The invertible neural network consists of 3 blocks, with each axis chosen in order. A 2D hash encoding is used with a size of 2^{19} and a maximum resolution of 1024^2 . The MLP has 2 hidden layers, each with 128 units. Additionally, we reconstruct the surface with NeuS2 [55] and generate the initial tetrahedral mesh through fTetWild [21]. We train each model with 30,000 iterations, which takes approximately 1 hour. The final model has an average of 826k tetrahedra with 197k vertices (for the *NeRF Synthetic* dataset). All experiments are conducted on a single GTX RTX4090 GPU.

Table 1. Quantitative results with different constraints.

	PSNR \uparrow	SSIM \uparrow	LPIPS \downarrow
w/o constraint	30.41	0.947	0.062
w/ \mathcal{L}_{volume}	29.37	0.925	0.076
w/ \mathcal{L}_{sv}	29.92	0.936	0.069
ours	<u>30.23</u>	<u>0.944</u>	<u>0.065</u>

Table 2. Quantitative results for different initializations.

	<i>lego</i>		<i>hotdog</i>		<i>mic</i>	
	PSNR \uparrow	SSIM \uparrow	PSNR \uparrow	SSIM \uparrow	PSNR \uparrow	SSIM \uparrow
w/ uniform	33.19	0.969	36.12	0.975	35.78	0.986
w/ NeuS2	35.48	0.982	37.69	0.985	37.56	0.993

4.1. Ablation Study

In this section, we conduct two main ablation studies to address the following questions:

- Q1: How much does our orientation-preserving homeomorphism affect rendering quality and mesh quality?
- Q2: Does an initially low-quality mesh degrade our reconstruction quality?

Q1: Effect of Orientation-preserving Homeomorphism.

We conduct this experiment using the *NeRF synthetic* dataset, with the mesh initialized by NeuS2 as input. To avoid the influence of adaptive control on the experiment, we removed this module, fixing the number of tetrahedra. We regularized the training of the tetrahedral mesh using four different methods: without constraints, with \mathcal{L}_{volume} , with \mathcal{L}_{sv} , and with our orientation-preserving homeomorphism as a constraint. Tab. 1 shows the quantitative results for the reconstruction of these four methods. Compared to the unconstrained optimization, our module has minimal impact on the rendering quality, whereas the other regularization terms significantly degrade the reconstruction quality. As shown in Fig. 7, under unconstrained conditions, the mesh exhibits a large number of overlaps and abnormal structures. Additionally, \mathcal{L}_{sv} and \mathcal{L}_{volume} constraints fail to effectively regulate the mesh structure. Since the local orientation-preserving property near the vertices cannot guarantee global inversion-free tetrahedra, our final result still contains a small number of inverted elements. Nonetheless, our method produces much better tetrahedral meshes compared to the constraints imposed by the loss function and achieves similar reconstruction quality as the unconstrained approach.

Q2: Ablations on Initial Mesh. We conduct this experiment on three scenes from the *NeRF synthetic* dataset: Lego, Hotdog, Mic. Initially, we start with a uniform tetrahedral mesh as described in Sec. 3.3, and project the tetra-

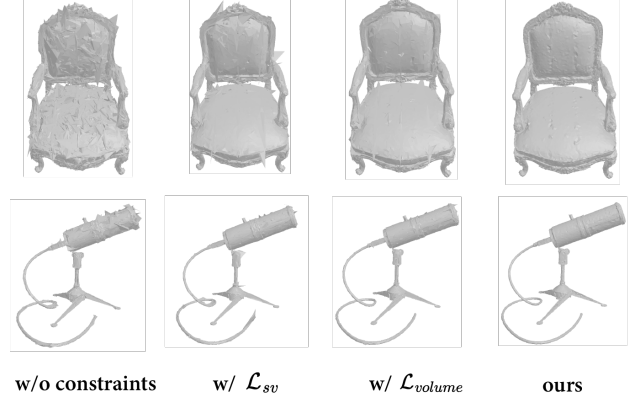


Figure 7. Visualization of tetrahedral mesh optimized with different constraints.

Table 3. Quantitative results on *NeRF Synthetic* and *Shelly* dataset.

	<i>NeRF Synthetic</i>			<i>Shelly</i>		
	PSNR \uparrow	SSIM \uparrow	LPIPS \downarrow	PSNR \uparrow	SSIM \uparrow	LPIPS \downarrow
NeRF	31.00	0.947	0.081	31.28	0.893	0.157
Adaptive Shells	31.84	0.957	0.056	36.02	0.954	0.079
3DGS	33.78	0.969	<u>0.030</u>	<u>39.61</u>	<u>0.961</u>	<u>0.064</u>
2DGS	32.92	0.966	0.036	34.62	0.928	0.098
Mani-GS	32.58	0.961	0.034	-	-	-
SuGaR	29.78	0.948	0.055	31.19	0.943	0.080
Ours	<u>33.53</u>	<u>0.968</u>	0.019	39.76	0.967	0.052

hedra onto the image plane, followed by tetrahedron pruning according to the mask. This tetrahedral mesh is then used as input to our method for training. Tab. 2 shows the final reconstruction results, compared to those obtained with NeuS2 initialization. Our method still produces good mesh quality and comparable reconstruction results, indicating that our approach is robust to mesh initialization.

4.2. Comparison

We conduct experiments to compare the performance of rendering on static scenes. The results show that, despite the need to maintain a structured geometry during optimization, we are still able to achieve comparable result to that of unstructured radiance field representation like 3DGS [30].

We employ two datasets for evaluation: *NeRF Synthetic* dataset [39], containing eight scenes, and *Shelly* dataset [57], containing six scenes. We conduct comparisons with implicit, point-based, and mesh-based methods to evaluate the performance of our approach, including NeRF [39], 3DGS [30], 2DGS [22], Adaptive Shells [57] and Mani-GS [17]. We use surface reconstructed by NeuS2 as input to Mani-GS for a fair comparison. We use the same training process as 3DGS. The rendering quality is evaluated using a set of established metrics: PSNR, SSIM [56],

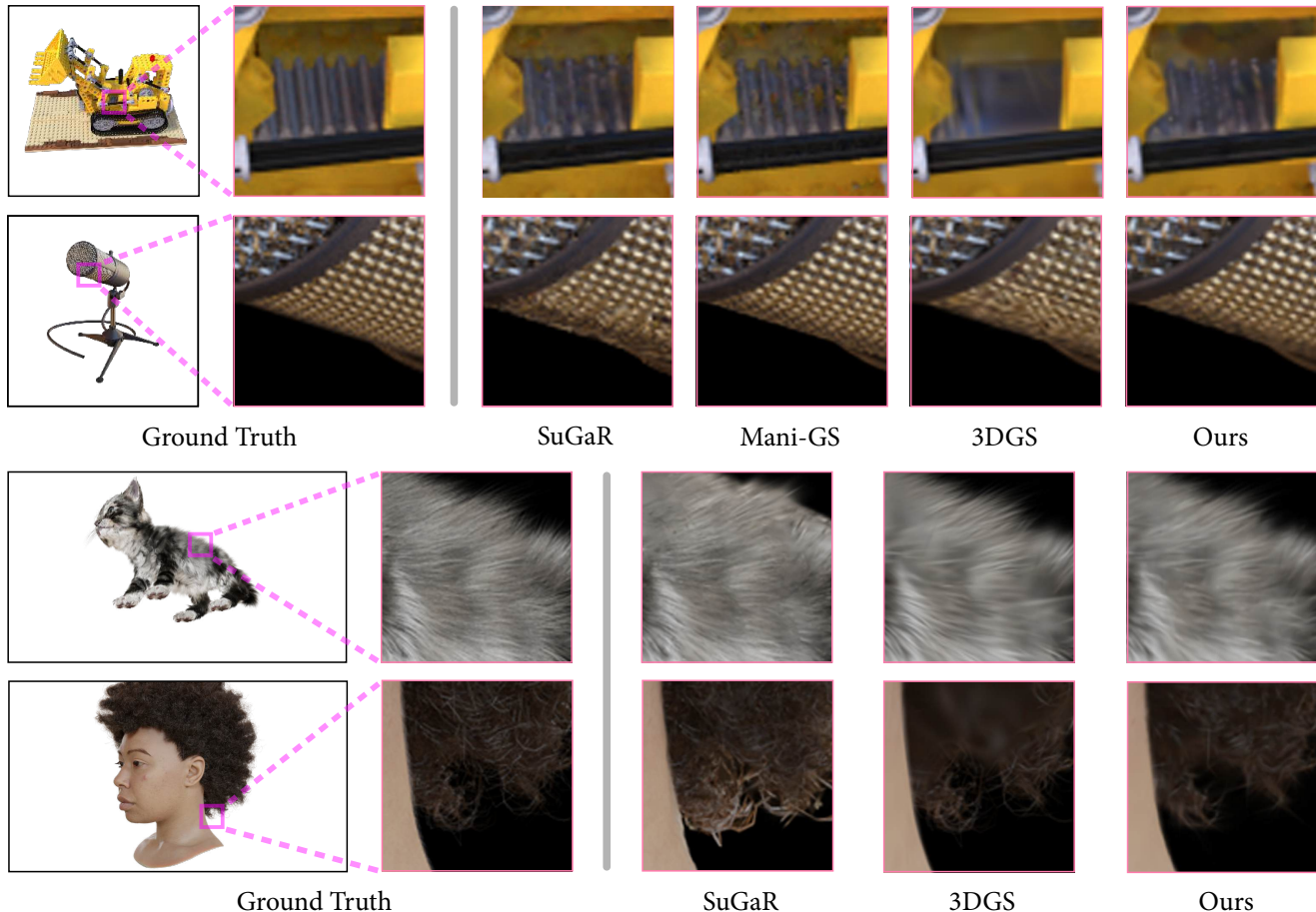


Figure 8. Our results on the test-views of *Shelly* dataset and *NeRF Synthetic* dataset.

and LPIPS [66]. In Tab. 3, we conduct a quantitative comparison of rendering quality. Our approach shows competitive results across all mesh-based and point-based methods according to three evaluation metrics. Moreover, our approach achieves qualitatively better reconstructions, with fewer artifacts and more detailed results, as shown in Fig. 8.

4.3. Applications

Our method directly constructs an explicit tetrahedral mesh \mathcal{M} with good quality, and achieves good rendering quality at the same time, which proves highly valuable for a variety of downstream applications. With tetrahedral mesh, we can perform physics simulations, animations, editing, and other operations seamlessly. With our proposed StructuredField, we can easily update the mesh by simply tracking the movement or displacement of each vertex. This allows us to reparameterize the Gaussians based on the new positions of vertices, enabling the rendering of deformed scenes.

Methods like Mani-GS and GaMes are hybrid representations that fix mesh vertex positions and establish a relationship between triangle meshes and 3D Gaussians. In

contrast, our method offers a unified, structured representation where the vertex positions are optimized during the reconstruction process. Since the final meshes produced by our method differ from those in hybrid methods, it is difficult to establish a fair comparison under the same deformation.

For many applications such as physical simulation and deformation, the tetrahedral mesh representation in our StructuredField has inherent advantages. Unlike triangle mesh, which only represent the surface of an object, tetrahedral mesh have internal structure, making it more suitable for physically accurate simulations. On the other hand, thanks to our carefully designed reparameterization strategy, the primitives in our representation are always confined within the corresponding tetrahedra. This ensures that our representation accurately reflects the mesh deformation. In contrast, previous methods using triangle mesh may suffer from artifacts during deformation, as the 3D Gaussians could shift away from the triangular surfaces, leading to potential inconsistencies between 3D Gaussians and triangle mesh.

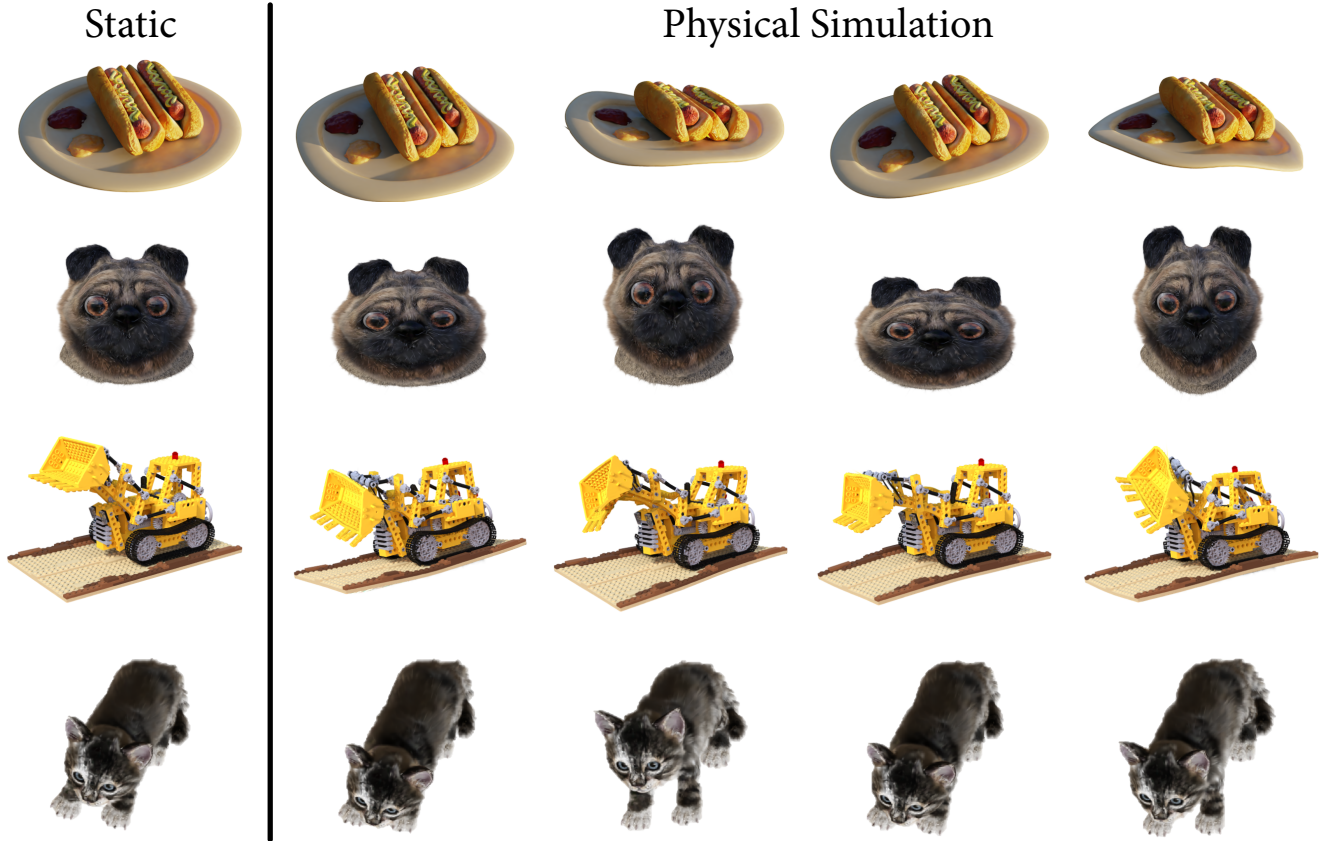


Figure 9. **Gallery of physical simulation results.** The original shape is shown in the leftmost column, with the corresponding physical simulations displayed in the right column. Videos are provided in the supplementary materials for further visualization.

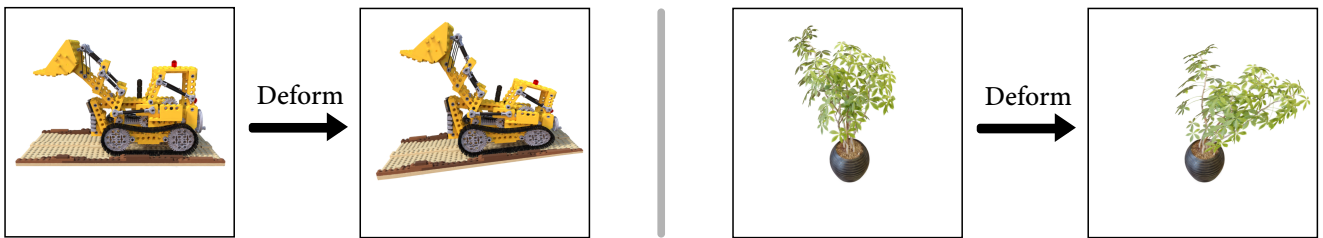


Figure 10. **Gallery of deformation results.** Videos are provided in the supplementary materials for further visualization.

Physical Simulation After constructing the tetrahedral mesh, we treat it as a mass-spring system, where each vertex is modeled as a mass point, and the edges serve as springs connecting these points. To simulate the physical behavior of the system, we implement the XPBD [37] (Extended Position Based Dynamics) algorithm using Taichi [20] programming language. Specifically, we apply constraints to preserve the spring lengths and tetrahedral volumes during the simulation, ensuring realistic deformations and interactions. Fig. 9 shows the results of our physics simulation: please refer to the supplemental video for dynamic motion. By adjusting various parameters of the object, such as mass

and the strength of spring constraints, we can simulate different effects on the same object.

Deformation We utilize lattice deformation as a mechanism to drive the deformation of the tetrahedral mesh. As the mesh vertices undergo deformation, we reparameterize the associated Gaussian primitives based on the updated positions of the mesh vertices. As demonstrated in Fig. 10 even under large-scale deformations, our representation still produces reasonable rendering results.

5. Conclusion

We introduced StructuredField, a novel structured 3D representation that unifies high-fidelity rendering and structured geometry. Our main contribution is using reparameterization to make tetrahedral mesh rendering differentiable. An orientation-preserving homeomorphism has been proposed to ensure the mesh quality during optimization. Extensive experiments have been conducted to verify the effectiveness of StructuredField on the aspects of rendering quality, physics simulations and deformation modeling.

Limitations Although our proposed StructuredField representation can simultaneously recover high-quality rendering and structured geometry from multi-view images, there are still some limitations: First, during the training process, vertices need to pass through the neural network, which leads to longer training time than unstructured radiance field representation. In addition, since we need to maintain structured geometry during the reconstruction process, our solution space is more restricted than unstructured radiance field representation, so more number of primitives are required to represent the scene to achieve similar rendering effects.

References

- [1] Hervé Abdi and Lynne J Williams. Principal component analysis. *Wiley interdisciplinary reviews: computational statistics*, 2(4):433–459, 2010. 4
- [2] Sameer Agarwal, Noah Snavely, Ian Simon, Steven M. Seitz, and Richard Szeliski. Building rome in a day. In *2009 IEEE 12th International Conference on Computer Vision*, pages 72–79, 2009. 2
- [3] Ryoichi Ando, Nils Thürey, and Chris Wojtan. Highly adaptive liquid simulations on tetrahedral meshes. *ACM Transactions on Graphics (TOG)*, 32(4):1–10, 2013. 1
- [4] David Baraff and Andrew Witkin. Large steps in cloth simulation. In *Seminal Graphics Papers: Pushing the Boundaries, Volume 2*, pages 767–778. 2023. 1
- [5] Jonathan T Barron, Ben Mildenhall, Matthew Tancik, Peter Hedman, Ricardo Martin-Brualla, and Pratul P Srinivasan. Mip-nerf: A multiscale representation for anti-aliasing neural radiance fields. In *Proceedings of the IEEE/CVF international conference on computer vision*, pages 5855–5864, 2021. 1, 2
- [6] Jonathan T Barron, Ben Mildenhall, Dor Verbin, Pratul P Srinivasan, and Peter Hedman. Mip-nerf 360: Unbounded anti-aliased neural radiance fields. In *Proceedings of the IEEE/CVF conference on computer vision and pattern recognition*, pages 5470–5479, 2022. 2
- [7] Jonathan T Barron, Ben Mildenhall, Dor Verbin, Pratul P Srinivasan, and Peter Hedman. Zip-nerf: Anti-aliased grid-based neural radiance fields. In *Proceedings of the IEEE/CVF International Conference on Computer Vision*, pages 19697–19705, 2023. 2
- [8] Jens Behrmann, Will Grathwohl, Ricky TQ Chen, David Duenaud, and Jörn-Henrik Jacobsen. Invertible residual networks. In *International conference on machine learning*, pages 573–582. PMLR, 2019. 1, 3
- [9] Mario Botsch, Alexander Hornung, Matthias Zwicker, and Leif Kobbelt. High-quality surface splatting on today’s gpus. In *2nd Symposium on Point Based Graphics, PBG 2005, Stony Brook, NY, USA, June 21-22, 2005*, pages 17–24, 2005. 1
- [10] Hongrui Cai, Wanquan Feng, Xuetao Feng, Yan Wang, and Juyong Zhang. Neural surface reconstruction of dynamic scenes with monocular rgb-d camera. *Advances in Neural Information Processing Systems*, 35:967–981, 2022. 3
- [11] Anpei Chen, Zexiang Xu, Andreas Geiger, Jingyi Yu, and Hao Su. Tensorf: Tensorial radiance fields. In *European conference on computer vision*, pages 333–350. Springer, 2022. 1
- [12] Laurent Dinh, Jascha Sohl-Dickstein, and Samy Bengio. Density estimation using real NVP. In *International Conference on Learning Representations (ICLR)*, 2017. 1, 3, 5
- [13] Jan-Michael Frahm, Pierre Fite-Georgel, David Gallup, Tim Johnson, Rahul Raguram, Changchang Wu, Yi-Hung Jen, Enrique Dunn, Brian Clipp, Svetlana Lazebnik, and Marc Pollefeys. Building rome on a cloudless day. In *Proceedings of the 11th European Conference on Computer Vision: Part IV*, page 368–381, Berlin, Heidelberg, 2010. Springer-Verlag. 2
- [14] Xiao-Ming Fu, Jian-Ping Su, Zheng-Yu Zhao, Qing Fang, Chunyang Ye, and Ligang Liu. Inversion-free geometric mapping construction: A survey. *Computational Visual Media*, 7:289–318, 2021. 3
- [15] Yasutaka Furukawa and Jean Ponce. Accurate, dense, and robust multiview stereopsis. *IEEE Transactions on Pattern Analysis and Machine Intelligence*, 32(8):1362–1376, 2010. 2
- [16] Yasutaka Furukawa, Brian Curless, Steven M. Seitz, and Richard Szeliski. Towards internet-scale multi-view stereo. In *2010 IEEE Computer Society Conference on Computer Vision and Pattern Recognition*, pages 1434–1441, 2010. 2
- [17] Xiangjun Gao, Xiaoyu Li, Yiyu Zhuang, Qi Zhang, Wenbo Hu, Chaopeng Zhang, Yao Yao, Ying Shan, and Long Quan. Mani-gs: Gaussian splatting manipulation with triangular mesh. *arXiv preprint arXiv:2405.17811*, 2024. 3, 7
- [18] Jan Held, Renaud Vandeghen, Abdullah Hamdi, Adrien Deliege, Anthony Cioppa, Silvio Giancola, Andrea Vedaldi, Bernard Ghanem, and Marc Van Droogenbroeck. 3d convex splatting: Radiance field rendering with 3d smooth convexes. *arXiv preprint arXiv:2411.14974*, 2024. 1, 4
- [19] Hugues Hoppe. Progressive meshes. In *Seminal Graphics Papers: Pushing the Boundaries, Volume 2*, pages 111–120. 2023. 1
- [20] Yuanming Hu, Tzu-Mao Li, Luke Anderson, Jonathan Ragan-Kelley, and Frédo Durand. Taichi: a language for high-performance computation on spatially sparse data structures. *ACM Trans. Graph.*, 38(6), 2019. 9
- [21] Yixin Hu, Teseo Schneider, Bolun Wang, Denis Zorin, and Daniele Panozzo. Fast tetrahedral meshing in the wild. *ACM Transactions on Graphics (ToG)*, 39(4):117–1, 2020. 6

- [22] Binbin Huang, Zehao Yu, Anpei Chen, Andreas Geiger, and Shenghua Gao. 2d gaussian splatting for geometrically accurate radiance fields. In *SIGGRAPH 2024 Conference Papers*. Association for Computing Machinery, 2024. 1, 3, 4, 7
- [23] Yi-Hua Huang, Ming-Xian Lin, Yang-Tian Sun, Ziyi Yang, Xiaoyang Lyu, Yan-Pei Cao, and Xiaojuan Qi. Deformable radial kernel splatting. *arXiv preprint arXiv:2412.11752*, 2024. 1, 3
- [24] Clément Jambon, Bernhard Kerbl, Georgios Kopanas, Stavros Diolatzis, Thomas Leimkühler, and George Drettakis. Nerfshop: Interactive editing of neural radiance fields. *Proceedings of the ACM on Computer Graphics and Interactive Techniques*, 6(1), 2023. 3
- [25] Doug L James and Christopher D Twigg. Skinning mesh animations. *ACM Transactions on Graphics (TOG)*, 24(3): 399–407, 2005. 1
- [26] Ying Jiang, Chang Yu, Tianyi Xie, Xuan Li, Yutao Feng, Huamin Wang, Minchen Li, Henry Lau, Feng Gao, Yin Yang, et al. Vr-gs: A physical dynamics-aware interactive gaussian splatting system in virtual reality. In *ACM SIGGRAPH 2024 Conference Papers*, pages 1–1, 2024. 3
- [27] Zhongshi Jiang, Scott Schaefer, and Daniele Panozzo. Simplicial complex augmentation framework for bijective maps. *ACM Transactions on Graphics*, 36(6), 2017. 3
- [28] Hailin Jin, Stefano Soatto, and Anthony J. Yezzi. Multi-view stereo reconstruction of dense shape and complex appearance. *International Journal of Computer Vision*, 63:175–189, 2005. 2
- [29] Nikhil Keetha, Jay Karhade, Krishna Murthy Jatavallabhula, Gengshan Yang, Sebastian Scherer, Deva Ramanan, and Jonathon Luiten. Splatam: Splat track & map 3d gaussians for dense rgb-d slam. In *Proceedings of the IEEE/CVF Conference on Computer Vision and Pattern Recognition*, pages 21357–21366, 2024. 2
- [30] Bernhard Kerbl, Georgios Kopanas, Thomas Leimkühler, and George Drettakis. 3d gaussian splatting for real-time radiance field rendering. *ACM Transactions on Graphics*, 42(4), 2023. 1, 2, 3, 4, 6, 7
- [31] Jonas Kulhanek and Torsten Sattler. Tetra-nerf: Representing neural radiance fields using tetrahedra. In *Proceedings of the IEEE/CVF International Conference on Computer Vision*, pages 18458–18469, 2023. 3
- [32] Jiahui Lei and Kostas Daniilidis. Cadex: Learning canonical deformation coordinate space for dynamic surface representation via neural homeomorphism. In *Proceedings of the IEEE/CVF Conference on Computer Vision and Pattern Recognition*, pages 6624–6634, 2022. 3
- [33] Jiaqi Lin, Zhihao Li, Xiao Tang, Jianzhuang Liu, Shiyong Liu, Jiayue Liu, Yangdi Lu, Xiaofei Wu, Songcen Xu, Youliang Yan, et al. Vastgaussian: Vast 3d gaussians for large scene reconstruction. In *Proceedings of the IEEE/CVF Conference on Computer Vision and Pattern Recognition*, pages 5166–5175, 2024. 2
- [34] Shichen Liu, Tianye Li, Weikai Chen, and Hao Li. Soft rasterizer: A differentiable renderer for image-based 3d reasoning. In *Proceedings of the IEEE/CVF international conference on computer vision*, pages 7708–7717, 2019. 1, 2
- [35] Tiantian Liu, Adam W Bargteil, James F O’Brien, and Ladislav Kavan. Fast simulation of mass-spring systems. *ACM Transactions on Graphics (TOG)*, 32(6):1–7, 2013. 1
- [36] Kwan-Liu Ma and Thomas W Crockett. A scalable parallel cell-projection volume rendering algorithm for three-dimensional unstructured data. In *Proceedings of the IEEE symposium on Parallel rendering*, pages 95–ff, 1997. 1
- [37] Miles Macklin, Matthias Müller, and Nuttapon Chentanez. Xpbd: position-based simulation of compliant constrained dynamics. In *Proceedings of the 9th International Conference on Motion in Games*, page 49–54, New York, NY, USA, 2016. Association for Computing Machinery. 9
- [38] Ben Mildenhall, Pratul P. Srinivasan, Matthew Tancik, Jonathan T. Barron, Ravi Ramamoorthi, and Ren Ng. Nerf: Representing scenes as neural radiance fields for view synthesis. In *ECCV*, 2020. 2
- [39] Ben Mildenhall, Pratul P. Srinivasan, Matthew Tancik, Jonathan T. Barron, Ravi Ramamoorthi, and Ren Ng. Nerf: Representing scenes as neural radiance fields for view synthesis. In *European Conference on Computer Vision (ECCV)*, 2020. 1, 2, 7
- [40] Marek Krzysztof Misztal and Jakob Andreas Bærentzen. Topology-adaptive interface tracking using the deformable simplicial complex. *ACM Transactions on Graphics (TOG)*, 31(3):1–12, 2012. 3
- [41] Thomas Müller, Alex Evans, Christoph Schied, and Alexander Keller. Instant neural graphics primitives with a multiresolution hash encoding. *ACM transactions on graphics (TOG)*, 41(4):1–15, 2022. 1, 2
- [42] Yicong Peng, Yichao Yan, Shengqi Liu, Yuhao Cheng, Shanyan Guan, Bowen Pan, Guangtao Zhai, and Xiaokang Yang. Cagenerf: Cage-based neural radiance field for generalized 3d deformation and animation. *Advances in Neural Information Processing Systems*, 35:31402–31415, 2022. 3
- [43] Stanislav Pidhorskyi, Tomas Simon, Gabriel Schwartz, He Wen, Yaser Sheikh, and Jason Saragih. Rasterized edge gradients: Handling discontinuities differentially. In *European Conference on Computer Vision*, pages 335–352. Springer, 2025. 2
- [44] Michael Rabinovich, Roi Poranne, Daniele Panozzo, and Olga Sorkine-Hornung. Scalable locally injective mappings. *ACM Transactions on Graphics (TOG)*, 36(4):1, 2017. 3
- [45] Christian Reiser, Stephan Garbin, Pratul Srinivasan, Dor Verbin, Richard Szeliski, Ben Mildenhall, Jonathan Barron, Peter Hedman, and Andreas Geiger. Binary opacity grids: Capturing fine geometric detail for mesh-based view synthesis. *ACM Transactions on Graphics (TOG)*, 43(4):1–14, 2024. 3
- [46] Radu Alexandru Rosu and Sven Behnke. Permutosdf: Fast multi-view reconstruction with implicit surfaces using permutohedral lattices. In *Proceedings of the IEEE/CVF Conference on Computer Vision and Pattern Recognition*, pages 8466–8475, 2023. 3
- [47] Szymon Rusinkiewicz and Marc Levoy. Qsplat: A multiresolution point rendering system for large meshes. In *Proceedings of the 27th annual conference on Computer graphics and interactive techniques*, pages 343–352, 2000. 1

- [48] Christian Schüller, Ladislav Kavan, Daniele Panozzo, and Olga Sorkine-Hornung. Locally injective mappings. In *Computer Graphics Forum*, pages 125–135. Wiley Online Library, 2013. 3, 5
- [49] Olga Sorkine and Marc Alexa. As-rigid-as-possible surface modeling. In *Symposium on Geometry processing*, pages 109–116. Citeseer, 2007. 1
- [50] Matthew Tancik, Vincent Casser, Xinchun Yan, Sabeek Pradhan, Ben Mildenhall, Pratul P Srinivasan, Jonathan T Barron, and Henrik Kretzschmar. Block-nerf: Scalable large scene neural view synthesis. In *Proceedings of the IEEE/CVF Conference on Computer Vision and Pattern Recognition*, pages 8248–8258, 2022. 2
- [51] Jiayang Tang, Jiawei Ren, Hang Zhou, Ziwei Liu, and Gang Zeng. Dreamgaussian: Generative gaussian splatting for efficient 3d content creation. In *International Conference on Learning Representations (ICLR)*, 2024. 2
- [52] Haithem Turki, Vasu Agrawal, Samuel Rota Bulò, Lorenzo Porzi, Peter Kotschieder, Deva Ramanan, Michael Zollhöfer, and Christian Richardt. Hybridnerf: Efficient neural rendering via adaptive volumetric surfaces. In *Proceedings of the IEEE/CVF Conference on Computer Vision and Pattern Recognition*, pages 19647–19656, 2024. 3
- [53] Ziyu Wan, Christian Richardt, Aljaž Božič, Chao Li, Vijay Rengarajan, Seonghyeon Nam, Xiaoyu Xiang, Tuotuo Li, Bo Zhu, Rakesh Ranjan, et al. Learning neural duplex radiance fields for real-time view synthesis. In *Proceedings of the IEEE/CVF Conference on Computer Vision and Pattern Recognition*, pages 8307–8316, 2023. 3
- [54] Peng Wang, Lingjie Liu, Yuan Liu, Christian Theobalt, Taku Komura, and Wenping Wang. Neus: Learning neural implicit surfaces by volume rendering for multi-view reconstruction. In *Advances in Neural Information Processing Systems 34: Annual Conference on Neural Information Processing Systems 2021, NeurIPS 2021, December 6-14, 2021, virtual*, pages 27171–27183, 2021. 3
- [55] Yiming Wang, Qin Han, Marc Habermann, Kostas Daniilidis, Christian Theobalt, and Lingjie Liu. Neus2: Fast learning of neural implicit surfaces for multi-view reconstruction. In *Proceedings of the IEEE/CVF International Conference on Computer Vision*, pages 3295–3306, 2023. 6
- [56] Zhou Wang, Alan C Bovik, Hamid R Sheikh, and Eero P Simoncelli. Image quality assessment: from error visibility to structural similarity. *IEEE transactions on image processing*, 13(4):600–612, 2004. 7
- [57] Zian Wang, Tianchang Shen, Merlin Nimier-David, Nicholas Sharp, Jun Gao, Alexander Keller, Sanja Fidler, Thomas Müller, and Zan Gojcic. Adaptive shells for efficient neural radiance field rendering. *ACM Trans. Graph.*, 42(6):260:1–260:15, 2023. 3, 7
- [58] Manfred Weiler, Martin Kraus, Markus Merz, and Thomas Ertl. Hardware-based view-independent cell projection. *IEEE Transactions on Visualization and Computer Graphics*, 9(2):163–175, 2003. 1
- [59] Mason Woo, Jackie Neider, Tom Davis, and Dave Shreiner. *OpenGL programming guide: the official guide to learning OpenGL, version 1.2*. Addison-Wesley Longman Publishing Co., Inc., 1999. 2
- [60] Jun Xiang, Xuan Gao, Yudong Guo, and Juyong Zhang. Flashavatar: High-fidelity head avatar with efficient gaussian embedding. In *Proceedings of the IEEE/CVF Conference on Computer Vision and Pattern Recognition*, pages 1802–1812, 2024. 2
- [61] Roni Yagel, David M Reed, Asish Law, Po-Wen Shih, and Naeem Shareef. Hardware assisted volume rendering of unstructured grids by incremental slicing. In *Proceedings of 1996 Symposium on Volume Visualization*, pages 55–62. IEEE, 1996. 1
- [62] Guandao Yang, Serge Belongie, Bharath Hariharan, and Vladlen Koltun. Geometry processing with neural fields. In *Thirty-Fifth Conference on Neural Information Processing Systems*, 2021. 3
- [63] Lior Yariv, Peter Hedman, Christian Reiser, Dor Verbin, Pratul P Srinivasan, Richard Szeliski, Jonathan T Barron, and Ben Mildenhall. Baked sdf: Meshing neural sdf for real-time view synthesis. In *ACM SIGGRAPH 2023 Conference Proceedings*, pages 1–9, 2023. 3
- [64] Wang Yifan, Felice Serena, Shihao Wu, Cengiz Öztireli, and Olga Sorkine-Hornung. Differentiable surface splatting for point-based geometry processing. *ACM Transactions on Graphics (TOG)*, 38(6):1–14, 2019. 1
- [65] Yizhou Yu, Kun Zhou, Dong Xu, Xiaohan Shi, Hujun Bao, Baining Guo, and Heung-Yeung Shum. Mesh editing with poisson-based gradient field manipulation. In *ACM SIGGRAPH 2004 Papers*, pages 644–651. 2004. 1
- [66] Richard Zhang, Phillip Isola, Alexei A Efros, Eli Shechtman, and Oliver Wang. The unreasonable effectiveness of deep features as a perceptual metric. In *Proceedings of the IEEE conference on computer vision and pattern recognition*, pages 586–595, 2018. 8
- [67] Wojciech Zielonka, Timur Bagautdinov, Shunsuke Saito, Michael Zollhöfer, Justus Thies, and Javier Romero. Drivable 3d gaussian avatars. In *International Conference on 3D Vision (3DV)*, 2025. 3
- [68] Denis Zorin, Peter Schröder, and Wim Sweldens. Interactive multiresolution mesh editing. In *Proceedings of the 24th annual conference on Computer graphics and interactive techniques*, pages 259–268, 1997. 1